Title
Hall effect anomaly and low-temperature metamagnetism in the Kondo compound CeAgBi2

Authors
Thomas, SM
Rosa, PFS
Lee, SB
et al.

Peer reviewed

Hall effect anomaly and low-temperature metamagnetism in the Kondo compound CeAgBi$_2$

S. M. Thomas, P. F. S. Rosa, S. B. Lee, S. A. Parameswaran, Z. Fisk, and J. Xia

Department of Physics and Astronomy, University of California, Irvine, California 92697-4574, USA

(Received 4 September 2015; revised manuscript received 5 February 2016; published 25 February 2016)

Heavy fermion (HF) materials exhibit a rich array of phenomena due to the strong Kondo coupling between their localized moments and itinerant electrons. A central question in their study is to understand the interplay between magnetic order and charge transport, and its role in stabilizing new quantum phases of matter. Particularly promising in this regard is a family of tetragonal intermetallic compounds CeTX_2 (where T denotes transition metal and X denotes pnictogen), which includes a variety of HF compounds showing T-linear electronic specific heat $\mathbf{C}_e \sim \gamma T$, with $\gamma \sim 20$–500 mJ mol^{-1} K^{-2}, reflecting an effective-mass enhancement ranging from small to modest. Here, we study the low-temperature field-tuned phase diagram of high-quality CeAgBi$_2$ using magnetometry and transport measurements. We find an antiferromagnetic transition at $T_N = 6.4$ K with weak magnetic anisotropy and the easy axis along the c axis, similar to previous reports ($T_N = 6.1$ K). This scenario, along with the presence of two anisotropic Ruderman-Kittel-Kasuya-Yosida interactions, leads to a rich field-tuned magnetic phase diagram, consisting of five metamagnetic transitions of both first and second order. In addition, we unveil an anomalous Hall contribution for fields $H < 54$ kOe, which is drastically altered when H is tuned through a trio of transitions at 57, 78, and 84 kOe, suggesting that the Fermi surface is reconstructed in a subset of the metamagnetic transitions.

In heavy fermion (HF) materials, the Kondo coupling between local moments and itinerant electrons plays a central role in determining magnetic and transport properties, particularly at low temperatures. Classic examples of the unusual behavior include quantum criticality in YbRh$_2$Si$_2$ [1], unconventional superconductivity in CeCoIn$_5$ [2], and metamagnetism in CeRu$_2$Si$_2$ [3]. Ce-based HF materials that host such exciting properties often crystallize in tetragonal structures, and their ground state is on the border of antiferromagnetism (AFM).

Our focus in this paper is the HF family CeTX_2 (where T denotes transition metal and X denotes pnictogen), a class of intermetallic compounds that crystallize in the tetragonal ZrCuSi$_2$-type structure (space group $P4/nmm$) with a stacking arrangement of CeX-T-CeX-X layers. Great attention has been given to the antimonide (X represents Sb) members due to the presence of anomalous ferromagnetism in CeAgSb$_2$ and, more recently, due to the report of field-induced quantum criticality in CeAuSb$_2$ [4,5]. Although the investigation of the antimonides is abundant, fewer reports can be found on the bismuthide (X represents Bi) members. Recent studies of high-quality CeCuBi$_2$ and CeAuBi$_2$ revealed AFM ordering temperatures of $T_N = 16$ and 12 K, respectively. Both materials show a moderate mass enhancement from T-linear electronic specific heat (γ on the order of 100 mJ mol^{-1} K^{-2}), and they exhibit a single spin-flop transition with field applied along the c axis [6,7].

CeAgBi$_2$, a third member of the isovalent series, has been reported previously to order antiferromagnetically ($T_N = 6.1$ K) at zero magnetic field and to undergo three field-induced magnetic transitions at 2 K ($H_c = 35$, 50, and 83 kOe) [8,9]. However, a detailed analysis of the underlying interactions and a deep understanding of the phase diagram at low temperatures is still missing.

Single crystals of CeAgBi$_2$ were grown from Bi flux with starting composition Ce:Ag:Bi = 1 : x_{nominal} : 8 ($1 \leqslant x_{\text{nominal}} \leqslant 3$). The mixture was placed in an alumina crucible and sealed in a quartz tube under vacuum. The sealed tube was heated up to 1050 °C for 8 h and then cooled down at 10 °C/h. The excess of Bi flux was removed by centrifugation after 24 h of annealing at 500 °C. Single crystals with dimensions $\sim 3 \times 3 \times 0.5$ mm^3 were ground and their crystal structure was checked by x-ray powder-diffraction experiments using Cu $K\alpha$ radiation at room temperature. Several single crystals from different batches were also submitted to elemental analysis using a commercial energy-dispersive spectroscopy (EDS) microprobe coupled to a field-emission gun scanning electron microscope (FEG SEM). From the EDS analysis, we have extracted the actual x_{Ag} concentration. The precision of the analysis was calculated by $\sigma/\sqrt{N}$, where σ is the standard deviation of the measurements and N is the number of points analyzed.

Magnetization measurements were performed using a commercial superconducting quantum interference device (SQUID) down to 1.8 K. Below 1.8 K, cantilever-based torque magnetometry was used to measure the magnetization in a dilution refrigerator. Electrical resistivity measurements were made using a low-frequency ac resistance bridge and a four-point configuration. Hall data were obtained by measuring in both positive and negative applied fields and taking the difference ($[R(H+) - R(H-)]/2$). Due to hysteresis in the transitions, data were paired for subtraction based on whether the magnitude of the field was increasing or decreasing. All measurements reported here, except for some of the magnetic susceptibility measurements, were performed with the applied field parallel to the c axis. For resistivity measurements, the current was applied in the ab plane.

I. EXPERIMENTAL RESULTS AND CEF FITS

Figure 1(a) shows the temperature dependence of in-plane resistivity, $\rho(T)$, down to 0.5 K at zero magnetic field. At high temperatures ($T \gtrsim 200$ K), $\rho(T)$ shows metallic behavior, decreasing linearly with decreasing temperature. However, a further decrease in temperature reveals a resistivity minimum, followed by a logarithmic increase due to incoherent Kondo
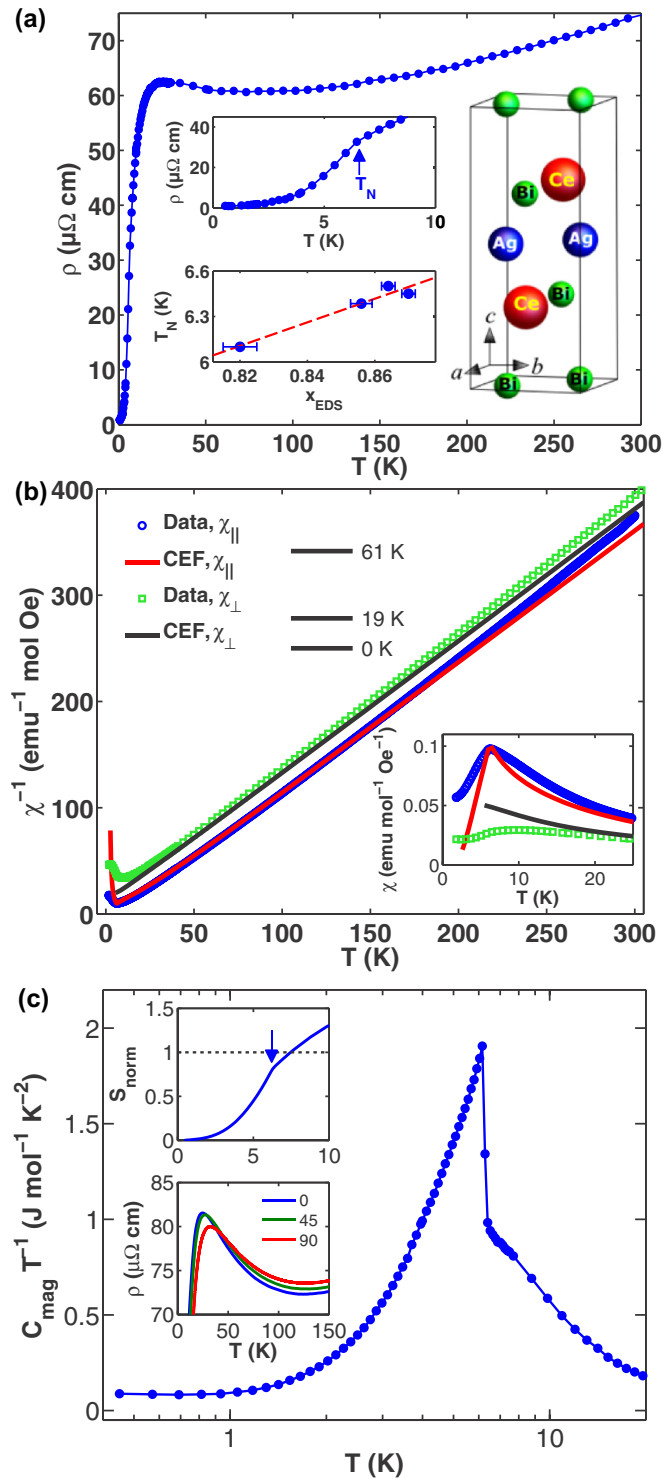
FIG. 1. (a) Temperature dependence of in-plane resistivity, $\rho(T)$, in zero applied field. The top inset shows the low-T region where a kink is observed at T_N. The bottom inset shows T_N as a function of Ag occupancy measured by EDS. (b) Inverse susceptibility data for fields parallel ($\chi_\parallel$) and perpendicular ($\chi_\perp$) to the c axis. The inset shows low-temperature $\chi(T)$ data. The solid lines are fits to the data using the model described in the text. (c) Magnetic contribution to specific heat in zero field. Top inset shows the integration of specific heat. S_{norm} is defined as $S/(R \ln 2)$. Bottom inset shows $\rho(T)$ in three different magnetic fields (in kOe).

scattering. Below ~ 25 K, $\rho(T)$ drops abruptly, suggesting that this is the energy scale of either CEF depopulation or Kondo coherence. We will discuss these possibilities below. The kink in resistivity observed at $T_N = 6.4$ K, shown in the top inset of Fig. 1(a), indicates the transition to the AFM phase. This represents a 0.3 K higher ordering temperature compared to previous studies of CeAgBi$_2$ [8,9]. Although this increase in T_N is somewhat small, EDS measurements reveal that it is caused by a substantial decrease both in the number of vacancies and in the inhomogeneity at the Ag site. The bottom inset of Fig. 1(a) shows the linear dependence of T_N on the occupation at the Ag site, x_{EDS}. For the most deficient samples, with Ag occupation of 82(4)%, the transition temperature matches previous studies, $T_N^{def} = 6.1$ K. For the best samples obtained to date, the Ag occupancy reaches 87(2)%, confirming the trend that transition-metal deficiency is an intrinsic feature of this family of compounds. We note that less deficient samples are also accompanied by higher resistance ratios and lower residual resistivity.

Like other Ce-based bismuthides, CeAgBi$_2$ also exhibits magnetic anisotropy. Figure 1(b) shows the temperature dependence of the inverse magnetic susceptibility, $1/\chi(T)$, when a magnetic field of $H = 1$ kOe is applied parallel ($\chi_\parallel$) and perpendicular ($\chi_\perp$) to the crystallographic c axis. The inset of Fig. 1(b) presents the low-temperature $\chi(T)$ data in which a sharp peak is observed at T_N. The ratio $\chi_\parallel/\chi_\perp \approx 3.5$ at T_N is mainly determined by the tetragonal CEF splitting and reflects the low-T Ce^{3+} single-ion anisotropy. This ratio is smaller than what is found in other bismuthides, suggesting a smaller CEF splitting between the ground state and the first excited state as well as a less anisotropic ground state. This scenario will be confirmed below.

At high temperatures ($T > 150$ K), $\chi(T)$ is well-described by a Curie-Weiss (CW) law plus a T-independent Pauli term, $\chi(T) = \chi_0 + C/(T - \theta_{CW})$. We obtain an effective moment of $\mu_{eff} \approx 2.5(1)\mu_B$ for both directions and also for the polycrystalline average, in agreement with the theoretical value of $\mu_{eff} \approx 2.54\mu_B$ for Ce^{3+} free ions. On the other hand, the θ_{CW} values are anisotropic, with $\theta_\parallel = 5.7$ K and $\theta_\perp = -8.5$ K. For the polycrystalline averaged data (not shown), we obtain $\theta_p = -4$ K, consistent with AFM order at ~ 6 K.

We now further explore the role of anisotropic interactions and CEF effects in the magnetic properties of CeAgBi$_2$. Toward that end, we analyze the experimental data using a mean-field model including two mean anisotropic interactions ($z_{AFM} J_{AFM}$ and $z_{FM} J_{FM}$) between nearest neighbors, which do not contain directional information. We also take into account the tetragonal CEF Hamiltonian $H_{CEF} = B_2^0 O_2^0 + B_4^0 O_4^0 + B_4^4 O_4^4$, where z is the number of nearest neighbors, B_i^n are the CEF parameters, and O_i^n are the Stevens equivalent operators obtained from the angular momentum operators. A more detailed description of the model can be found in Ref. [10].

This model was used to simultaneously fit $\chi(T)$, $M(H)$, and $C_{mag}(T)/T$ data in the entire range of temperature. The best fit that reproduces the anisotropic susceptibility is shown by solid lines in Fig. 1(b), and the extracted parameters for the CEF scheme and the exchange interactions are given in Table I. We find a $|J = 5/2, J_z = \pm 3/2\rangle$ Kramers doublet ground state, separated from other excited doublets by 19 and 60 K. We also find, in fact, (i) the CEF splitting is much smaller

TABLE I. CEF parameters, energy levels, and wave functions of $CeAgBi_2$ single crystals obtained from the best fits of the magnetic susceptibility data to the model described in the text.

CEF parameters (in K)					
B_2^0	B_4^0	B_4^4		$z_{FM} J_{FM}$	$z_{AFM} J_{AFM}$
-1.78	0.168	0.71×10^{-3}		-0.89	1.35
Energy levels and wave functions					
E (K)	$\lvert-5/2\rangle$	$\lvert-3/2\rangle$	$\lvert-1/2\rangle$	$\lvert+1/2\rangle$	$\lvert+3/2\rangle$	$\lvert+5/2\rangle$
0	0	-1	0	0	0	0
0	0	0	0	0	1	0
19	1	0	0	0	0	0
19	0	0	0	0	0	-1
61	0	0	-1	0	0	0
61	0	0	0	-1	0	0

as compared to other bismuthides, and (ii) the ground state is mainly $\lvert J = 5/2, J_z = \pm 3/2\rangle$ instead of the dominantly $\lvert J = 5/2, J_z = \pm 5/2\rangle$ found in $CeCuBi_2$ and $CeAuBi_2$. Further, the dominant CEF parameter B_2^0 obtained from the fits is similar to the value obtained using the high-temperature expansion of χ: $B_2^0 = 10(\theta_\perp - \theta_\parallel)/[3(2J - 1)(2J + 3)] = -1.48$ K [11]. This result suggests that the effects of anisotropic interactions at high temperatures are smaller in $CeAgBi_2$ than in $CeCuBi_2$ and $CeAuBi_2$. We also note that although the magnetic anisotropy and T_N along the c axis are well reproduced by our simple model, the single-ion CEF effect is not able to capture all field-induced transitions in $M(H)$ data at 1.8 K.

Figure 1(c) shows the temperature dependence of the specific heat of $CeAgBi_2$ in zero field. To determine the magnetic contribution to specific heat, the data obtained from the nonmagnetic reference compound $LaAgBi_2$ were subtracted from the result. There is a single peak corresponding to T_N. We note that this sample is from an earlier batch, so it has higher silver vacancies and a lower T_N. The top inset of Fig. 1(c) shows the integration of specific heat over temperature, i.e., the recovered magnetic entropy. At T_N, the recovered entropy is only about 80% of the ground-state doublet ($R \ln 2$). We note, however, that there is a broad feature centered around 8 K, which is consistent with a Schottky anomaly generated by the CEF splitting of 19 K. This result indicates that the first-excited CEF state is already partially occupied at T_N, giving an additional entropy to the expected $R \ln 2$. Therefore, the reduction of entropy is larger than 20%, although a precise calculation cannot be evaluated. It is unlikely that a reduction of entropy of more than 20% can be fully accounted for by classical magnetic fluctuations. For example, numerical calculations of the Ising model on a simple cubic lattice find an entropy reduction of just under 20% at T_N, with other three-dimensional geometries showing an even smaller reduction [12]. We thus attribute this reduction to both magnetic frustration and hybridization between Ce $4f$ electrons and conduction electrons. This conclusion is motivated by the enhanced effect masses found in dHvA experiments [8] and the magnetic frustration that often arises from competing exchange interactions.

Due to the similar energy scales of the first-excited CEF state (19 K) and the peak in resistance (24 K), we performed
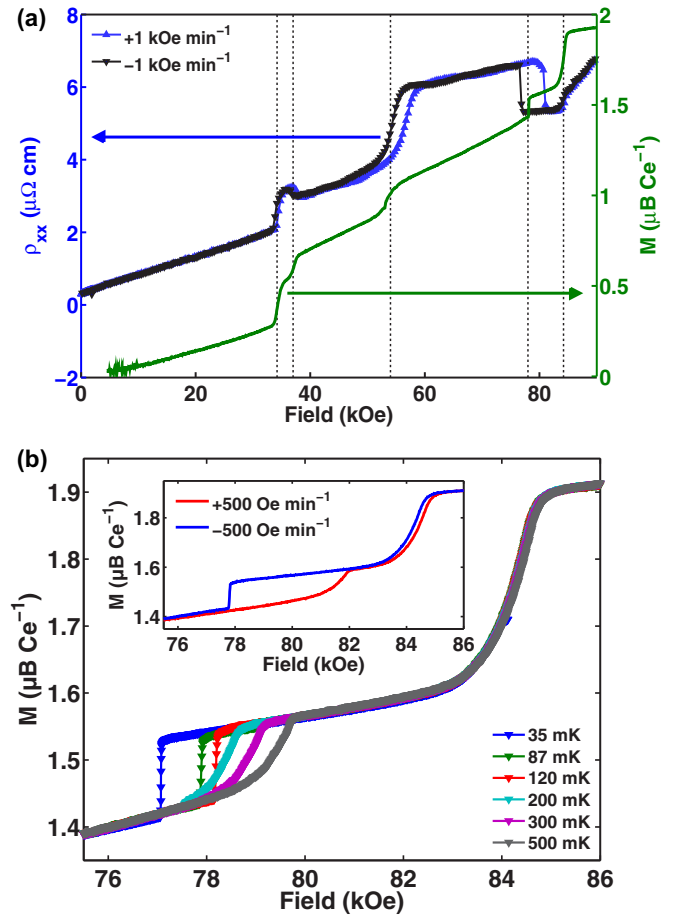

FIG. 2. Field-tuned magnetic and transport properties of $CeAgBi_2$. (a) ρ_{xx} (blue) and magnetization (green) vs field at 100 mK. ρ_{xx} data are for both increasing and decreasing fields, showing hysteresis for transitions centered near 54 and 78 kOe. (b) Magnetization vs field for decreasing field-sweep at temperatures 500 mK and lower. Sweep rate was 500 Oe/min. The inset shows hysteresis in magnetization depending on field-sweep direction.

high-temperature resistance measurements in several different fields. The results are presented in the inset of Fig. 1(c). If the peak near 24 K were due to crystal-field depopulation, then increasing the field should lead to an increase of the energy difference between the lowest Zeeman split state of the ground state and the upper Zeeman split state of the first-excited CEF state. This in turn would lead to an increase in the temperature of the resistance peak as the field is increased, which is in fact observed experimentally. We note that, in heavy fermion compounds where the energy difference between Kondo coherence and Δ_{CEF} is small, the onset of Kondo coherence (T^*) usually occurs at temperatures of the order of $\Delta_{CEF}/2$. This suggests that $T^* \sim 10$ K in $CeAgBi_2$. However, the experimental lack of two distinct resistance maxima, as is typically observed when the energy difference is large [13], leads to an ambiguity as to whether the resistance peak is due to CEF splitting of Kondo coherence.

We now turn to the analysis of the low-temperature phase diagram as a function of an applied magnetic field along the c axis. Figure 2(a) shows magnetization and (transverse) magnetoresistance (MR) of $CeAgBi_2$ at 100 mK. As the field

is swept from 0 to 90 kOe, we find a sequence of field-induced metamagnetic transitions near $H = 34, 37, 54, 78$, and 84 kOe, indicating a complex phase diagram for $T < T_N$. Above the 84 kOe transition, the magnetization saturates just below $1.9\mu_B/\text{Ce}$, which is slightly lower than the saturation value of $2.1\mu_B/\text{Ce}$ previously reported, and it may be due to a nonlinearity between the deflection of the cantilever and the corresponding change in capacitance. Such a large saturated value is somewhat surprising since the largest possible c-axis magnetization of a $|\pm3/2\rangle$ CEF ground state is $(3/2)g_L\mu_B$, i.e., $1.29\mu_B/\text{Ce}$. Hence, our results indicate that the Zeeman effect induces a change in the CEF ground state from $|\pm3/2\rangle$ to $|\pm5/2\rangle$ when $H \sim 84$ kOe.

Of the observed transitions, the one near 78 kOe appears to be strongly first-order, as shown by magnetization in Fig. 2(b). As T is lowered from 500 to 35 mK, a sharpening of the transition is observed and the transition eventually becomes steplike. Field sweeps performed around this transition show signs of irreversibility, namely an ~4-kOe-wide hysteresis loop, providing further evidence of first-order behavior. This is in contrast with other Ce-based bismuthides. For instance, other members of the isovalent series, such as CeCuBi$_2$ ($T_N = 16$ K) and CeAuBi$_2$ ($T_N = 12$ K), show only a single clear spin-flop transition. We note, however, that multiple steps have been observed in previous reports on more deficient CeCuBi$_2$ ($T_N = 11$ K), and even CeCuBi$_2$ ($T_N = 16$ K) shows hints of a second transition just before the main one. It is also noteworthy that hysteresis loops show a significant difference (~2 kOe) at the transition centered near 54 kOe as well. The change in magnetization, however, is not nearly as abrupt as that found in the 78 kOe transition. It is well known that transport measurements in real materials are complicated by disorder. Thus, as this transition is clearly not strongly first-order, the slight amount of irreversibility is likely attributed to pinning due to crystallographic defects (e.g., inherent silver deficiency). In fact, a small amount of hysteresis (on the order of 100 G) was also observed in magnetization and transport at the remaining three transitions.

The rich phase structure in CeAgBi$_2$ is likely due to the weak anisotropy combined with anisotropic exchange parameters with opposite signs, which lead to magnetic frustration. Further, the close energy scales of the CEF splitting (~19 K), Kondo coherence (~10 K), and AFM ($T_N \sim 6.4$ K) generates a complex response of the physical properties to the application of magnetic field.

The MR also reflects the multistep phase structure, tracking each metamagnetic transition with a sharp step, indicating the presence of Kondo coupling between the Ce magnetic moments and itinerant p electrons from Bi. The overall trend of MR is linear, a feature shared with the (nonmagnetic) compounds LaAgBi$_2$ and LaAgSb$_2$, where it is attributed to an underlying Dirac dispersion for Bi/Sb itinerant electrons [14,15]. A preliminary *ab initio* calculation [16] for CeAgBi$_2$ indicates that the Bi p electrons also have a Dirac dispersion, suggesting a similar origin for the underlying linear MR. However, we note that an alternative explanation for the increase in MR is an enhancement in spin-disorder scattering in AFM materials in an applied field [17,18]. Note that the MR exhibits a sharp drop and hysteretic behavior near the 79 kOe transition, lending further support that it is first-order.
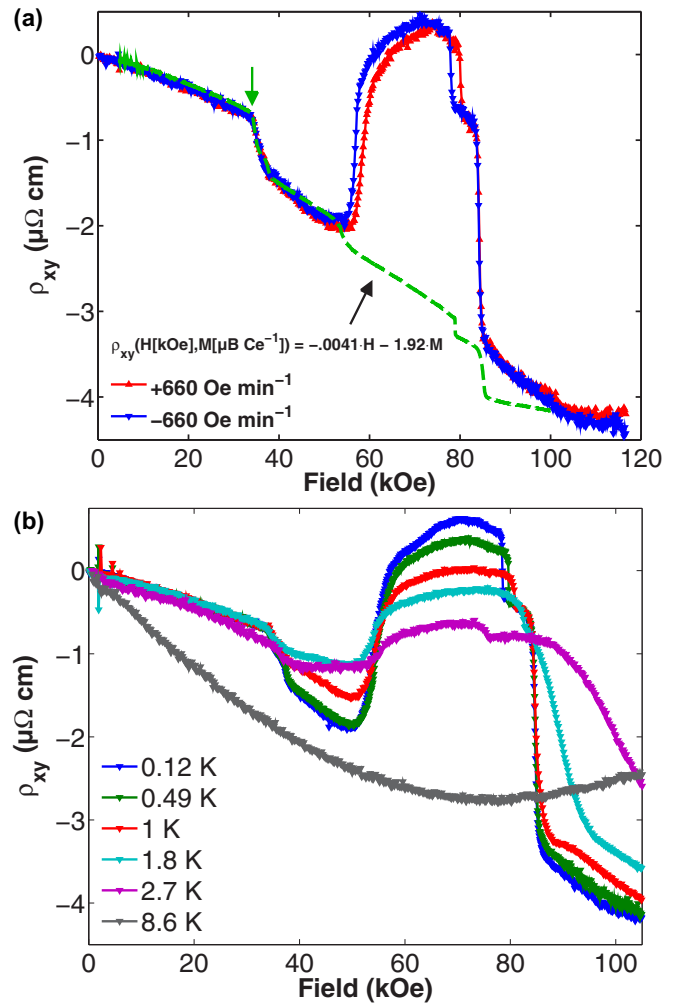

FIG. 3. Hall resistance (ρ_{xy}) vs field. (a) Comparison of sweeping the field up vs down at 150 mK. The dotted line is a least-squares fit to $\rho_{xy}(H) = R_H H + R_M M(H)$. The fit was made to the region of zero field up to 37 kOe (green arrow) and extrapolated beyond that point. (b) In a second sample, comparison was made at different T while sweeping the field downward.

Motivated by this evidence for coupling of itinerant electrons and local moments, we performed measurements of the Hall resistivity ρ_{xy} to further elucidate the nature of the different phases. Like the MR, the Hall effect tracks each metamagnetic transition (Fig. 3).

The decrease in ρ_{xy} roughly parallels the increase in magnetization over the first two transitions, but then sharply deviates from this trend as the field is increased across the trio of transitions at 57, 78, and 84 kOe, even changing its sign between ~60 and 80 kOe. Further insight is afforded by fitting the Hall resistivity to the standard form $\rho_{xy}(H) = R_H H + R_M M(H)$, which includes Hall effect contributions from both the applied field and the induced magnetization. Using the data up to $H \lesssim 38$ kOe to obtain the fit parameters, we find that this model fits the data extremely well for low fields $H \lesssim 54$ kOe, whereupon the measured ρ_{xy} strongly deviates from the expectation based on the model. While there is still some discrepancy between the fit and the data after the last
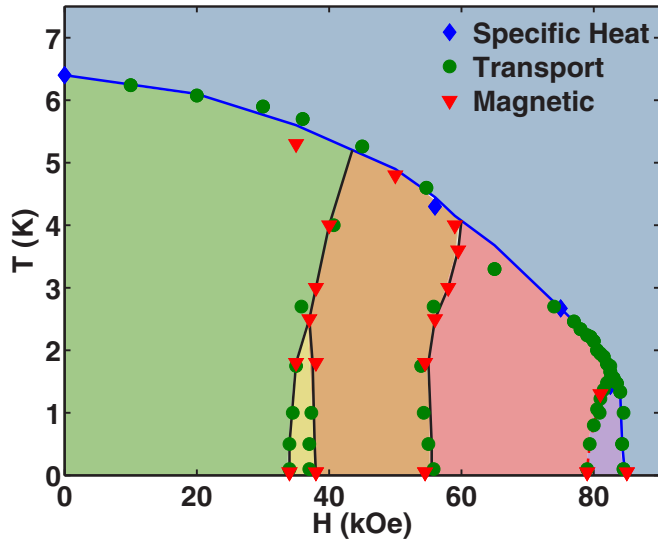
FIG. 4. (a) Low-temperature H-T phase diagram from CeAgBi2. The phase boundary was determined by resistivity, magnetization, and heat capacity measurements.

transition ($H \gtrsim 84$ kOe), this is relatively small compared to the much larger deviation between fit and data in the regime $54 \lesssim H \lesssim 84$ kOe. As the temperature is raised, the magnitude of the anomaly in ρ_{xy} near 54 kOe is decreased, as shown in Fig. 3(b). At present, we do not have a complete understanding of the origin of this Hall effect anomaly, but we comment on some possible scenarios below. We note that while there is an additional deviation from linear behavior of ρ_{xy} above $\sim$110 kOe, a previous study on lower-quality samples using pulsed fields up to 400 kOe [8] appears to rule out an additional transition.

II. DISCUSSION

Our results can be summarized in the form of a phase diagram of CeAgBi$_2$ with temperature and applied field, as shown in Fig. 4. The second $T = 0$ phase (for $34 < H < 37$ kOe) is not seen above the temperature $T \gtrsim 2.5$ K, illustrating the fragility of this phase to thermal fluctuations. Note the strong agreement between the probes of specific heat, transport, and magnetic structure when the corresponding measurements overlap. Of the sequence of transitions between the different low-temperature phases, the penultimate transition near 79 kOe appears to be strongly first-order, whereas the remaining transitions appear continuous. As noted, the Hall effect is well-described by a simple model including the effects of both the applied field and induced magnetization very well below 54 kOe and reasonably well above 84 kOe, but it exhibits a strong deviation from this simple behavior in the intermediate field regime.

Heavy fermion compounds CeAuSb$_2$ and YbAgGe both have some commonalities in the low-temperature phase diagram. For instance, CeAuSb$_2$ orders antiferromagnetically and has at least one magnetic transition before the suppression of AF order to 0 K at 54 kOe [5]. Recent work suggests that the first transition might bifurcate into two at lower temperatures, similar to CeAgBi$_2$ [19]. YbAgGe also has a

similarly complicated phase diagram as a function of field that contains a region partially bordered by a first-order transition [20]. Interestingly, in this region YbAgGe exhibits anomalous behavior attributed to the influence of a quantum bicritical point [21]. Unlike in YbAgGe, however, the set of transitions is only observed in CeAgBi$_2$ for $H \| c$. Further, the large anomalies in the Hall resistivity appear to be a feature unique to CeAgBi$_2$.

We now comment on potential explanations for the physics at hand. First, we attribute the sequence of metamagnetic transitions to the frustration from competing anisotropic exchange interactions, as evidenced by the susceptibility data. As in many HFs, the Hall data are more challenging to describe [22]. Their evident sensitivity to magnetization suggests a significant contribution from the induced magnetization at low fields, yet a simple phenomenological model incorporating this contribution seems to be unable to describe the behavior at intermediate fields. Here we note that quantum oscillation measurements reveal electron effective masses in the range of 5–7m_e, suggesting heavy fermion physics plays a role in transport [8]; this could perhaps explain the anomaly, e.g., via a Fermi surface reconstruction. To explore this scenario, one would have to investigate, for instance, band-structure calculations in the presence of a magnetic field. We anticipate that future theoretical analysis, incorporating details of the conduction electron band structure, as well as a careful treatment of their coupling to local moments, will shed more light on these issues [16].

An alternative scenario involves the "geometrical Hall effect" from a noncollinear spin texture; while more exotic, such physics is now quite well-established as a consequence of Dzyaloshinskii-Moriya interactions in ferromagnets and has also been proposed to occur in anisotropic exchange AFM, and recently also in heavy fermion metals [23]. In this case, an anomalous Hall effect could be observed as a result of a nonvanishing Berry-phase curvature [24]. Toward that end, neutron diffraction/scattering experiments would be valuable to unveil, for instance, the field regions where noncollinear spin structures are realized.

III. SPIN MODEL AND METAMAGNETIC TRANSITIONS

As mentioned above, our previous model was unable to capture all field-induced magnetic transitions. Finally, in the present section we introduce a spin model for the Ce local moments to discuss their field-induced response. Although more experimental investigation is clearly essential in order to clarify what type of AFM order is stabilized in CeAgBi$_2$ in each field region, here we sketch one possible scenario built upon existing experimental data on the closely related compound CeCuBi$_2$, where the zero-field magnetic structure has already been well-established experimentally [7]. We defer a detailed analysis of the spin model to future work, and here we discuss only a simple mean-field picture of the magnetic order.

For CeCuBi$_2$, x-ray magnetic diffraction reveals that the Ce local moments order antiferromagnetically with an ordering wave vector $(0,0,0.5)$ [7]. This corresponds to "up-up-down-down" magnetic ordering along the crystallographic c axis and ferromagnetic (FM) ordering across the basal a-b plane (see Fig. 5). The magnetic susceptibility data show a large
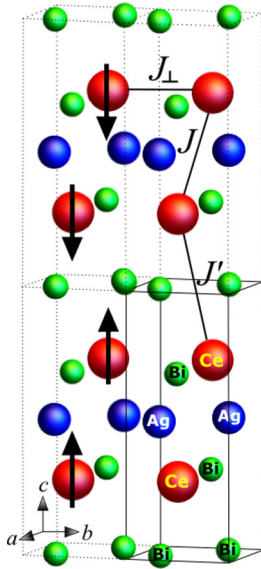
FIG. 5. Lattice structure of CeAgBi$_2$: Red, blue, and green spheres represent Ce, Ag, and Bi ions, respectively, and the solid line shows one unit cell. "Up-up-down-down"-like ordering of Ce moments is also shown along the c axis, which is measured to be the zero-field magnetic structure in CeCuBi$_2$. J, J', and $J_\perp$ indicates three symmetry-distinct spin exchange interactions between Ce magnetic moments.

anisotropy consistent with a strong easy axis along the c axis. The application of a c-axis magnetic field results in a single spin-flop transition at a field of $\sim$55 kOe; for fields in the ab plane, no such transition was observed. Within a classical approximation, a minimal spin model that may be inferred from these experimental results incorporates a single-ion anisotropy term and dominant spin exchanges between neighboring sites:

$$\mathcal{H} = \sum_{ij} J_{ij} \boldsymbol{S}_i \cdot \boldsymbol{S}_j - \sum_i \boldsymbol{h} \cdot \boldsymbol{S}_i - \Delta \sum_i \left(S_i^z\right)^2. \quad (1)$$

Here, $\boldsymbol{h}$ is the (applied) magnetic field and $\Delta > 0$ is the magnitude of an easy-axis single-ion anisotropy along the c axis. J_{ij} represents competing spin exchanges between neighboring sites; FM and AFM (or AFM and FM) spin exchanges for two symmetry-distinct neighbors along c axis are denoted J and J', respectively, and a FM spin interaction in the a-b plane is denoted as $J_\perp$, as seen in Fig. 5. The competition between alternating ferro- and antiferromagnetic spin exchanges along the c axis stabilizes the "up-up-down-down" magnetic structure along the c axis, with a spin-polarized state FM on each a-b plane. In the limit $\Delta \gg J_{ij}$, the moments behave like c-axis Ising spins, and the presence of a c-axis field leads to a direct magnetic transition from AF ordering to a fully-spin-polarized, paramagnetic state. However, a smaller single-ion anisotropy $\Delta \lesssim J_{ij}$ admits a spin-flop transition at a finite c-axis field, resulting in AF spin canting. This is consistent with the experimental data. Given that the minimal picture of competing spin exchanges and single-ion anisotropy provide a reasonable explanation of magnetic ordering and the field effect of CeCuBi$_2$ material, we now turn to a similar analysis of CeAgBi$_2$.

Magnetic susceptibility measurements on CeAgBi$_2$ again show the presence of magnetic anisotropy but smaller than in CeCuBi$_2$, which indicates weaker Ising anisotropy of the localized moments. Furthermore, when Ag substitutes for Cu on the transition-metal site, spin superexchange between Ce moments occurs via the 4d or 5s Ag orbitals, as compared to the 3d or 4s electrons of Cu, thereby changing the effective superexchange couplings $J, J', J_\perp$. Moreover, the slight difference in lattice parameters and bond angles may also lead to changes in the Ruderman-Kittel-Kasuya-Yosida interactions induced by coupling to the itinerant electrons of Bi. In general, this confluence of competing effects may stabilize very complicated magnetic ordering. We also note that further-neighbor interactions besides J, J', and $J_\perp$ generally induce incommensurate *spiral* ordering, affording an even richer set of possibilities. For the purposes of a preliminary analysis, we focus on our minimal spin model keeping just J, J', and $J_\perp$, and describing the possible ordered states as a function of the applied field. Notably, even this simple model exhibits a plethora of magnetic orders separated by a sequence of metamagnetic transitions.

A convenient approach to understanding the magnetic order is to separately consider every two layers of Ce sites, corresponding to a single unit-cell lattice spacing along the c axis. These two layers of Ce sites then form a buckled square lattice, where the nearest- and next-nearest-neighbor spin-spin couplings are J and $J_\perp$, respectively; we will refer to this as a "bilayer." Reasoning in analogy with the well-studied J_1-J_2 square-lattice Heisenberg model, we anticipate that FM, Néel, and stripy phases can be stabilized in each bilayer depending on the relative signs and magnitudes of J and $J_\perp$. We may then use these orders as a building block to construct the full three-dimensional magnetic order by coupling the Ce bilayers via an interlayer coupling J'. We now briefly summarize how competing interactions and magnetic anisotropy can lead to several metamagnetic transitions within this approach, even if we restrict ourselves to working within a classical spin approximation. To have several metamagnetic phases, we require that J, J', $J_\perp$, and Δ are all of the same order; this is also consistent with expectations based on experiments and a study of lattice parameters. To describe the ordered states stabilized with this parameter regime, it is convenient to work with a magnetic unit cell eight times larger than the original unit cell (i.e., containing 16 Ce sites), and to optimize the classical energy of this unit cell for a given set of parameters J_{ij}, Δ, and h, we minimize the energy of Eq. (1).

Figure 6 shows the magnetization m ($m = 1$ is the fully polarized classical spin per site) as a function of the c-axis magnetic field for specific values of parameters $J = -1$, $J' = 2$, $J_\perp = 1.5$, and $\Delta = 1$, which are the parameters that best describe the experimental data. In fact, we find six distinct phases over our field range. Note that the exact same argument can be applied when J and J' values are interchanged, due to site connectivity. The magnetic ordering pattern in each of these phases is illustrated in Fig. 7.

At zero field, each buckled square lattice bilayer forms a stripy phase, as $|J| < |J_\perp|$, and the stripy phase is robust under a small and finite magnetic field. With the chosen parameters, this phase is degenerate in energy with the "up-up-down-down"-like ordering (discussed for the case of
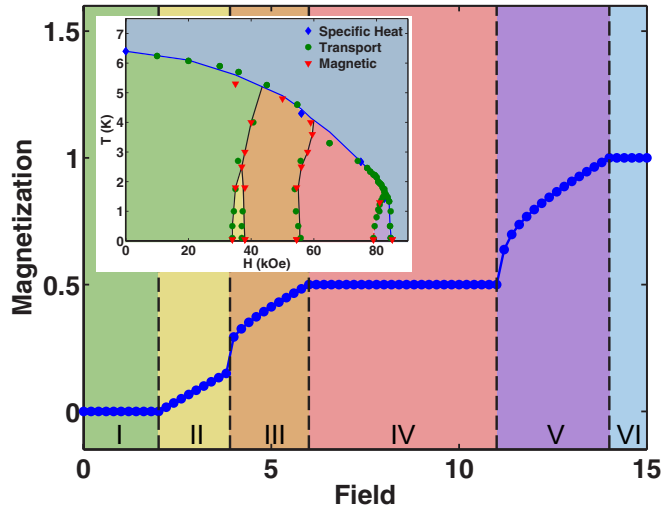
FIG. 6. Plot of magnetization m vs field h applied along the c axis. In the presence of competing spin exchange interactions and anisotropy, there exist several magnetic phases with applying fields. [In particular, we take $J = -1$, $J' = 2$, $J_\perp = 1.5$, and $\Delta = 1$ in Eq. (1).] Figure 7 describes different magnetic ordering patterns in every phase, (I)–(VI). The inset shows the experimental phase diagram from Fig. 4.

CeCuBi$_2$ and illustrated in Fig. 5). A further increase of magnetic field, however, induces a transition into a phase where spins in the lower two layers are polarized along the field direction, and spins in the upper two layers are antialigned to the field but have a finite canting. The canted moments induce a finite magnetization, preventing perfect cancellation of magnetic moments between the upper and lower bilayers. At $h \approx 4$, a partial spin-flop transition occurs, yielding a finite magnetization jump. In this phase, spins in the upper two layers almost form a stripy phase, similar to phase (I). In the lower two layers, however, all spins attempt to align along the field direction, but four spins form a different canting angle with respect to the other four. By smoothly changing those canting angles, this phase reaches a half-magnetization plateau region, where spins in the upper bilayer form a stripy phase, and spins in the lower bilayer are fully polarized. With stronger magnetic fields, there is another partial spin-flop transition exhibiting a finite jump in the magnetization. In phase (V), all 16 spins attempt to be aligned along the field direction, but four of them have a different canting angle until their canting angle becomes zero and a fully polarized spin state (VI) is realized at a saturation field $H \approx 14$.

Based on the above analysis, we conclude that competing exchange interactions and anisotropy can in principle lead to several metamagnetic transitions with field. We exemplified this for a specific parameter regime in Eq. (1), and we found six distinct phases that may emerge, taking into account the most dominant exchange interactions. Future neutron scattering studies will be valuable to confirm such a scenario and to establish a firmer foundation for theoretical studies. More detailed theoretical and experimental analyses will be discussed in Ref. [16], which will also discuss scenarios beyond this minimal model and attempt to connect the magnetic ordering with transport.
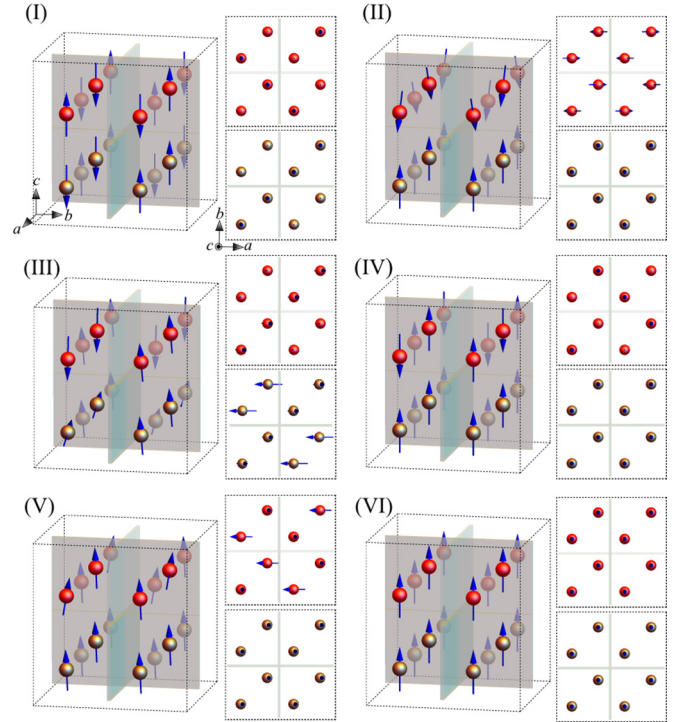

FIG. 7. Magnetic ordering patterns for the phases I–VI in Fig. 6. For a clear description of ordering patterns, three figures are shown for every phase: the figure on the left shows the ordering pattern in the 16-site magnetic unit cell, while the two figures on the right are top-down views of upper and lower Ce bilayers, respectively. (I) Spins in every bilayer form a stripy phase on a buckled square lattice. (II) Spins in the lower bilayer are polarized along the field direction, while spins in the upper bilayer cant in the field direction. A small canting induces finite magnetization m, as seen in Fig. 7. (III) Spins in the upper bilayer form a stripy phase, and four spins flop in the lower bilayer, resulting in a partial spin-flop transition with a finite magnetization jump at the transition point $h \approx 4$. (IV, Half-magnetization plateau region) Spins in the lower bilayer are polarized along the field direction, and spins in the upper bilayer form a stripy phase. (V) Spins in the lower bilayer are polarized, and four spins in the upper bilayer flop from a stripy phase, resulting in another partial spin-flop transition and magnetization jump near $h \approx 11$. (VI) All spins are fully polarized along the field direction beyond the saturation field.

IV. CONCLUSIONS

In conclusion, we have shown that high-quality CeAgBi$_2$ single crystals ($T_N = 6.4$ K) present a rich field-tuned phase diagram with five metamagnetic transitions at 40 mK. In contrast to other CeTX_2 members, a strongly first-order transition is observed at ~ 79 kOe in the vicinity of the transition to the paramagnetic state. Remarkably, we unveil an anomalous Hall contribution for fields $H < 54$ kOe, which is drastically altered when H is tuned through a trio of transitions at 57, 78, and 84 kOe, suggesting that the Fermi surface is reconstructed in a subset of the metamagnetic transitions. Our results shed light on hidden properties of CeAgBi$_2$ and open up new avenues for both experimental and theoretical studies on noncollinear magnetic structures, quantum (bi)criticality, and Fermi surface effects, to name a few.

[1] J. Custers, P. Gegenwart, H. Wilhelm, K. Neumaier, Y. Tokiwa, O. Trovarelli, C. Geibel, F. Steglich, C. Pépin, and P. Coleman, Nature (London) **424**, 524 (2003).

[2] R. Movshovich, M. Jaime, J. D. Thompson, C. Petrovic, Z. Fisk, P. G. Pagliuso, and J. L. Sarrao, Phys. Rev. Lett. **86**, 5152 (2001).

[3] R. Daou, C. Bergemann, and S. R. Julian, Phys. Rev. Lett. **96**, 026401 (2006).

[4] S. Araki, N. Metoki, A. Galatanu, E. Yamamoto, A. Thamizhavel, and Y. Onuki, Phys. Rev. B **68**, 024408 (2003).

[5] L. Balicas, S. Nakatsuji, H. Lee, P. Schlottmann, T. P. Murphy, and Z. Fisk, Phys. Rev. B **72**, 064422 (2005).

[6] C. Adriano, P. F. S. Rosa, C. B. R. Jesus, T. Grant, Z. Fisk, D. J. Garcia, and P. G. Pagliuso, J. Appl. Phys. **117**, 17C103 (2015).

[7] C. Adriano, P. F. S. Rosa, C. B. R. Jesus, J. R. L. Mardegan, T. M. Garitezi, T. Grant, Z. Fisk, D. J. Garcia, A. P. Reyes, P. L. Kuhns *et al.*, Phys. Rev. B **90**, 235120 (2014).

[8] A. Thamizhavel, A. Galatanu, E. Yamamoto, T. Okubo, M. Yamada, K. Tabata, T. C Kobayashi, N. Nakamura, K. Sugiyama, K. Kindo *et al.*, J. Phys. Soc. Jpn. **72**, 2632 (2003).

[9] C. Petrovic, S. Budko, J. Strand, and P. Canfield, J. Magn. Magn. Mater. **261**, 210 (2003).

[10] P. G. Pagliuso, D. J. Garcia, E. Miranda, E. Granado, R. Lora Serrano, C. Giles, J. G. S. Duque, R. R. Urbano, C. Rettori, J. D. Thompson *et al.*, J. Appl. Phys. **99**, 08P703 (2006).

[11] M. Avila, S. Bud'ko, and P. Canfield, J. Magn. Magn. Mater. **270**, 51 (2003).

[12] L. J. de Jongh, J. Appl. Phys. **49**, 1305 (1978).

[13] Y. Lassailly, A. K. Bhattacharjee, and B. Coqblin, Phys. Rev. B **31**, 7424 (1985).

[14] K. Wang, D. Graf, and C. Petrovic, Phys. Rev. B **87**, 235101 (2013).

[15] K. Myers, S. Bud'ko, I. Fisher, Z. Islam, H. Kleinke, A. Lacerda, and P. Canfield, J. Magn. Magn. Mater. **205**, 27 (1999).

[16] S. Lee, C.-J. Kang, S. Thomas, P. Rosa, B. Min, Z. Fisk, J. Xia, and S. Parameswaran (unpublished).

[17] C. Haas, Phys. Rev. **168**, 531 (1968).

[18] H. Yamada and S. Takada, J. Phys. Soc. Jpn. **34**, 51 (1973).

[19] K.-A. Lorenzer, A. M. Strydom, A. Thamizhavel, and S. Paschen, Phys. Status Solidi **250**, 464 (2013).

[20] S. L. Budko, E. Morosan, and P. C. Canfield, Phys. Rev. B **69**, 014415 (2004).

[21] Y. Tokiwa, M. Garst, P. Gegenwart, S. L. Budko, and P. C. Canfield, Phys. Rev. Lett. **111**, 116401 (2013).

[22] S. Nair, S. Wirth, S. Friedemann, F. Steglich, Q. Si, and A. J. Schofield, Adv. Phys. **61**, 583 (2012).

[23] W. Ding, S. Paschen, and Q. Si, arXiv:1507.07328.

[24] H. Chen, Q. Niu, and A. H. MacDonald, Phys. Rev. Lett. **112**, 017205 (2014).